Electronic Supplementary Information for

Redox Mo-Chloro-Species-Coupled Se Oxidation Conversion in Low-Corrosion Ionic Liquids for Fast-Kinetics and Durable Zn Batteries

Bo Wang,[ac] Yongchao Tang,*[ab] Jianping Yan,[a] Yufei Zhang,[a] Minghui Ye,[a] Zhipeng Wen,[a] Wencheng Du[ad], Xiaoqing Liu[a], and Cheng Chao Li*[a]

[a] School of Chemical Engineering and Light Industry, Guangdong University of Technology, Guangzhou, 510006, P. R. China

[b] Songshan Lake Materials Laboratory, Dongguan, 523808, P. R. China

[c] *Department of Physics, City University of Hong Kong, Hong Kong 999077, P. R. China*

[d] School of Advanced Manufacturing, Guangdong University of Technology, Jieyang 522000, P. R. China

Email: tyc@gdut.edu.cn, licc@gdut.edu.cn

1. Experimental Section

1.1 Synthesis of 1T-$MoSe_2$ cathode

The flower-like 1T-$MoSe_2$ nanosheets are obtained by a simple one-pot solvothermal synthesis. Typically, 0.8 mmol of $MoCl_5$ (99.5%, Macklin) and 1.6 mmol of SeO_2 (99.9%, Aladdin) powders were added into 50 mL of octylamine (99%, Aladdin) in a Teflon-lined autoclave (100 mL). After the solution was stirred for several minutes, the autoclave was sealed and kept in an oven at 180 ℃ for 12 h. The final product was obtained by freeze-drying method after washing with DI water several times.

1.2 Electrolyte Preparation

The $ZnCl_2$/EMImCl ionic liquid electrolyte was prepared by mixing $ZnCl_2$ (99.95%, Macklin) and 1-ethyl-3-methylimidazolium chloride (EMImCl, 98%, Macklin) with the different molar ratio of 1:1, 1.5:1, 1.8:1. Subsequently, the compound was stirred at 80℃ for 12 h. Finally, the $ZnCl_2$/EMImCl ionic liquid electrolyte was maintained at room temperature for 12 h before use. It is noted that the electrolyte was prepared in a glovebox filled with an argon atmosphere.

1.3 Materials characterization

XRD analysis was used to determine the phase structures of the samples with a Rigaku instrument (Cu Kα, λ= 1.5418 Å). The morphologies and microstructures were investigated by the SEM (Hitach-SU8220 field emission) and TEM (FEL-Talos F200S) with an energy dispersive spectroscopy (EDS). The chemical states of the sample and electrodes after testing were determined by XPS (Thermo Fisher-Escalab 250Xi), and binding energies were calibrated using carbon (284.8 eV for C 1s). Raman spectra (HORIBA, LabRAM HR Evolution) of the sample and electrolyte were measured at room temperature with laser excitation at 532 nm (for powder sample) and 785 nm (for electrolyte). The electrolyte viscosity was measured in a dry room environment utilizing an Anton-Paar MCR 102 rheometer, applying a constant shear rate of 10 s^{-1}, and using a Peltier system for temperature control. The viscosity values averaged over 5 min (150 data points) were used. The ionic conductivity was tested by an ionic conductivity meter (CM-25R, TOA-DKK). Time-of-flight secondary ion mass spectrometry (TOF-IMS) surface analysis was carried out with a TOF secondary ion mass spectrometer (TOF-SIMS ion tof Gmhb 5) equipped with a bismuth primary-ion source. The X-ray absorption near-edge structure (XANES) measurements were carried out on the sample at 21A X-ray nano diffraction beamline of Taiwan Photon Source (TPS), National Synchrotron Radiation Research Center (NSRRC). This beamline adopted a 4-bounce channel-cut Si (111) monochromator for mono-beam X-ray nano diffraction and X-ray absorption spectroscopy. The end-station is equipped with three ionization chambers and a Lytle/SDD detector after the focusing position of KB mirror for transmission and fluorescence mode X-ray absorption spectroscopy.

The photon flux on the sample ranges from 1×10^{11} to 3×10^{9} photon/sec for X-ray energy from 6-27 keV.

1.4 Electrochemical Measurements

Electrochemical testing was conducted on CR2032 coin-type cells in the voltage range of 0.1-2.3 V. The electrode was prepared by coating a slurry mixed the 1T-$MoSe_2$ or pure Se (70 wt%), Super P (20 wt%), and polyvinylidene fluoride (10 wt%) uniformly on a carbon paper current collector and dried at 80 °C for 12 h in a vacuum oven. The mass loading of active materials was 0.8-1.0 mg cm^{-2}. Metallic Zn foil (10 μm; Φ = 12 mm) as both counter and reference electrodes. Glass fiber (Whatman) was used as the separator. The appropriate amount of electrolyte (180-200 μL) was added. The batteries were assembled in a glove box under an argon atmosphere. The N/P ratio of the Zn-$MoSe_2$ coin-type battery is *ca.* 5.6. The galvanostatic charge-discharge and GITT tests were performed on the Neware battery test system (Shenzhen, China). The LSV, Tafel, CV curves, and EIS plots were tested on the Gamry electrochemical workstation, and the frequency of EIS ranged from 100 kHz to 0.01 Hz.

1.5 The preparation process of pouch batteries

For fabricating pouch cells, the cathode was prepared by coating a slurry mixed with the 1T-$MoSe_2$ powders (70 wt%), Super P (20 wt%), and polyvinylidene fluoride (10 wt%) uniformly on a carbon paper current collector (size: 3.5 cm × 3.5 cm), and dried at 80 °C for 12 h in a vacuum oven. The mass loading of active materials is 13-15 mg cm^{-2}. Zn foil with 10 μm thickness was used as the anode (size: 3.5 cm × 3.5 cm). Glass fiber (Whatman) was used as the separator. Then, the appropriate amount of electrolyte was added and the aluminum-plastic film shell was sealed by hot pressing in a vacuum sealing machine. The open circuit voltage of the pouch-battery was checked by multimeter to judge whether the battery is short-circuited. Finally, the Zn-$MoSe_2$ pouch batteries were left for 2 h before electrochemical testing. It is noted that the batteries were assembled in a glove box in an argon atmosphere.

1.6 Theoretical computations

All simulations were investigated using the density functional theory (DFT) of the Gaussian 09W program package. The geometric optimization and transition states calculations were performed by using B3LYP functional with SDD basis set for metal atoms and 6-31g(d) basis set for other atoms.[1] The single point energy was performed by using B3LYP functional with SDD basis set for metal atoms and 6-311+g(d) basis set for other atoms. DFT-D3(BJ) corrections were taken into consideration for each calculation.

2. Supplementary Figures

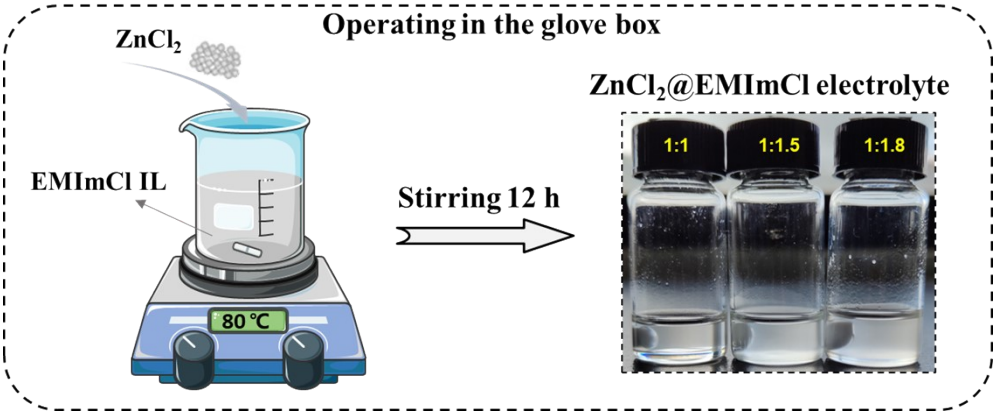

Fig. S1. The preparation schematic and the optical photographs of different molar ratios of $ZnCl_2$@EMImCl electrolyte electrolytes. The $ZnCl_2$/EMImCl ionic liquid electrolyte was prepared by mixing $ZnCl_2$ and 1-ethyl-3-methylimidazolium chloride with the different molar ratios of 1:1, 1.5:1, 1.8:1. Subsequently, the compound was stirred at 80 ℃ for 12 h. Finally, the $ZnCl_2$/EMImCl ionic liquid electrolyte was maintained at room temperature for 12 h before use.

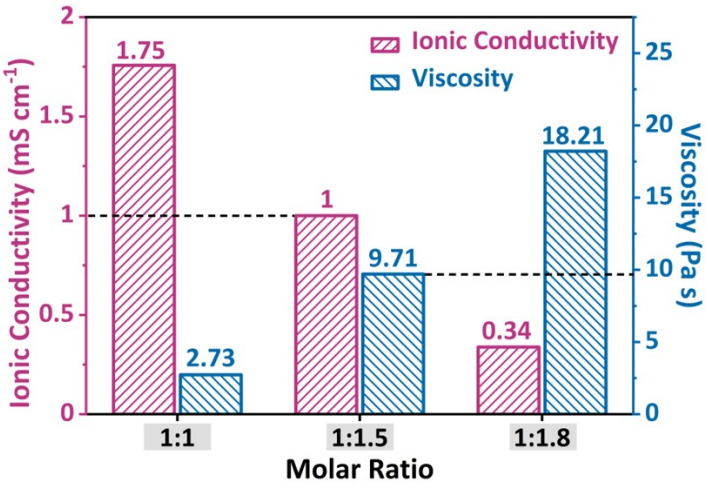

Fig. S2. The ionic conductivity and viscosity of $ZnCl_2$@EMImCl electrolyte at different ratios.

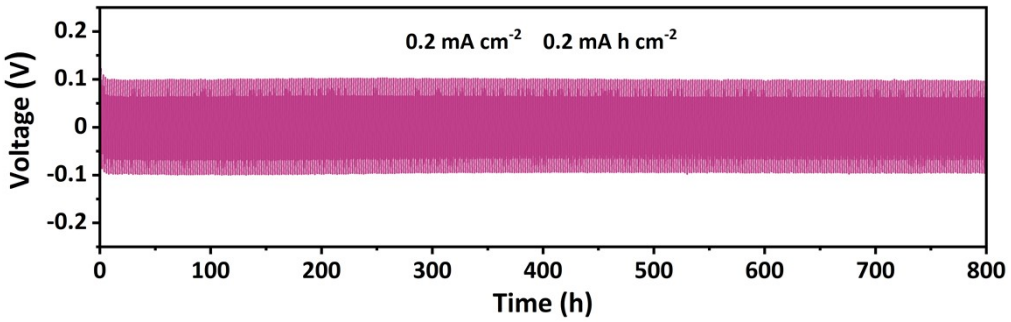

Fig. S3. The cycle performance of Zn||Zn symmetric batteries.

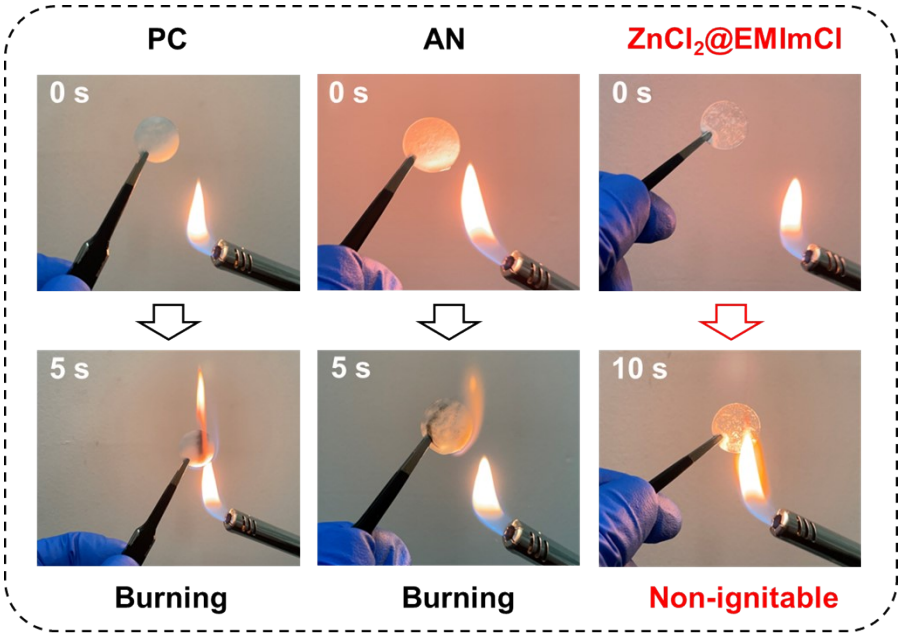

Fig. S4. Contrast photographs of the ignition test of PC, AN, and $ZnCl_2$@EMImCl electrolyte.

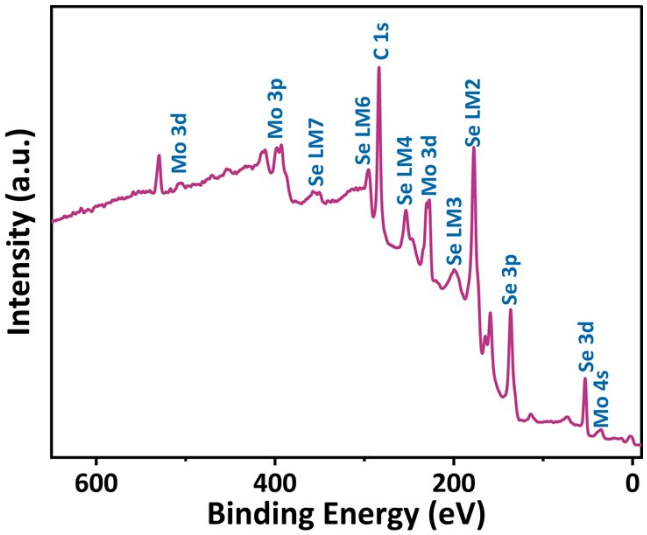

Fig. S5. The XPS survey spectrum of the 1T-$MoSe_2$ sample.

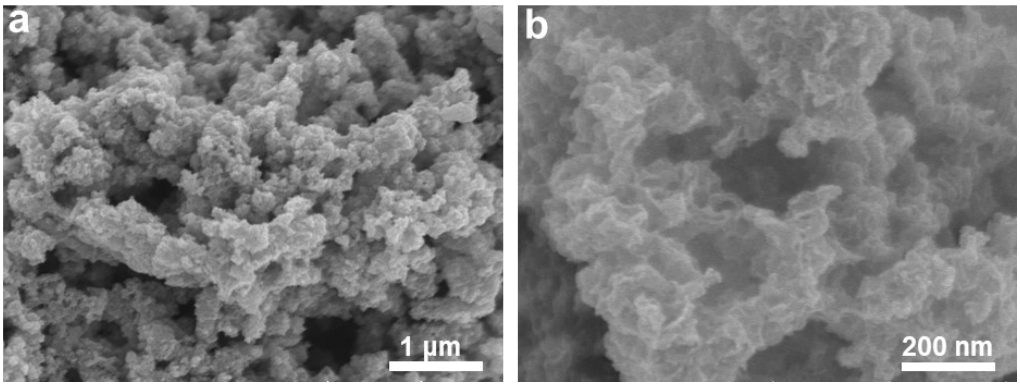

Fig. S6. The SEM images of the 1T-$MoSe_2$ sample.

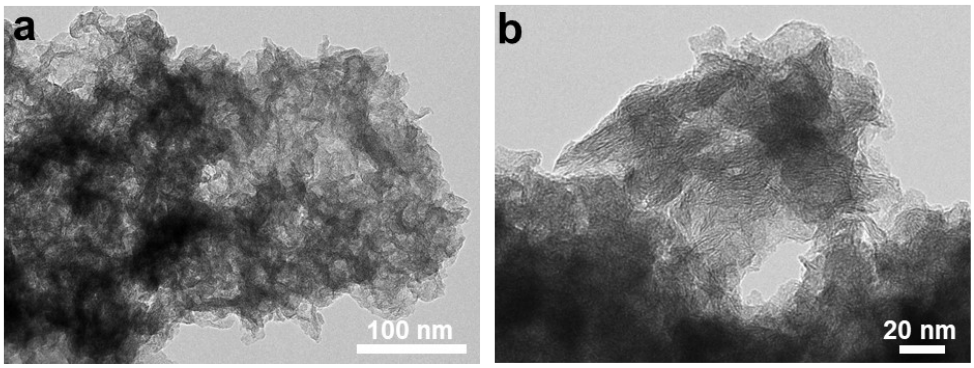

Fig. S7. The TEM images of the 1T-$MoSe_2$ sample.

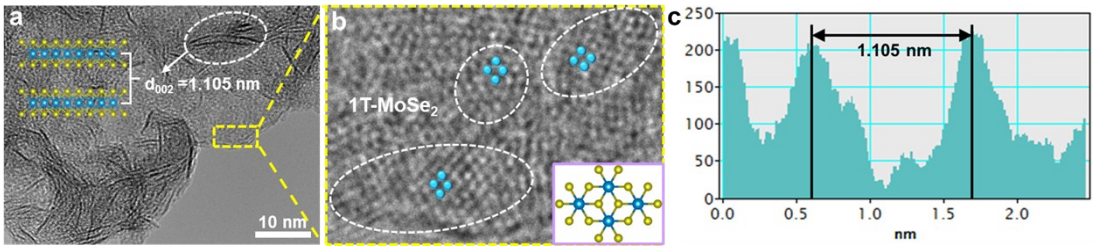

Fig. S8. The (a, b) HRTEM images and (c) *d*-spacing of (002) of 1T-$MoSe_2$ sample.

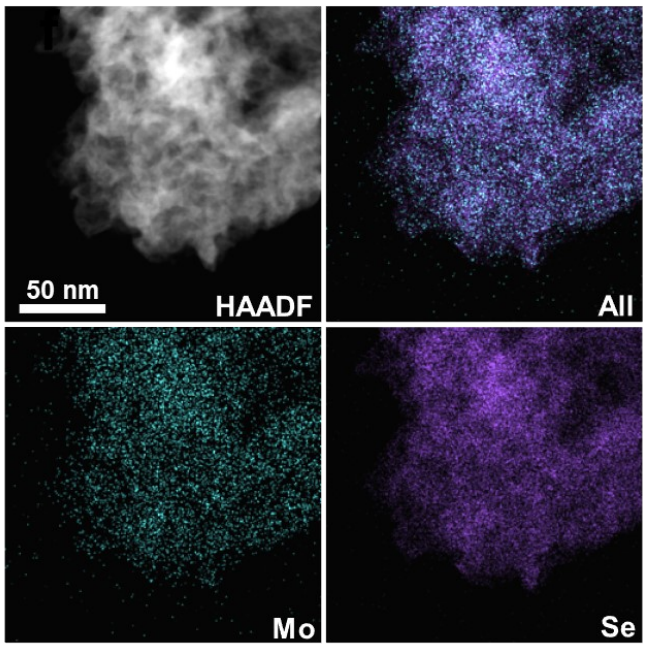

Fig. S9. The mapping images of the 1T-$MoSe_2$ sample.

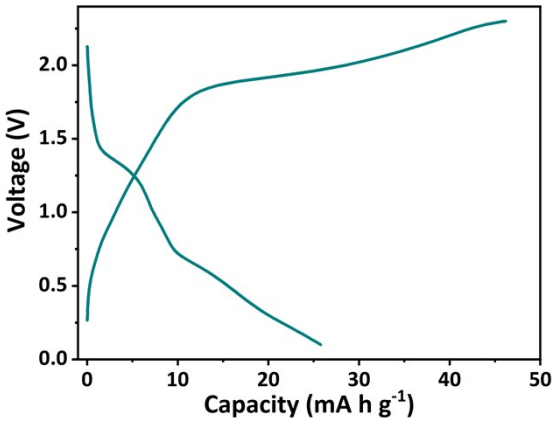

Fig. S10. The GCD curve of Mo electrodes at 0.5 A g^{-1}.

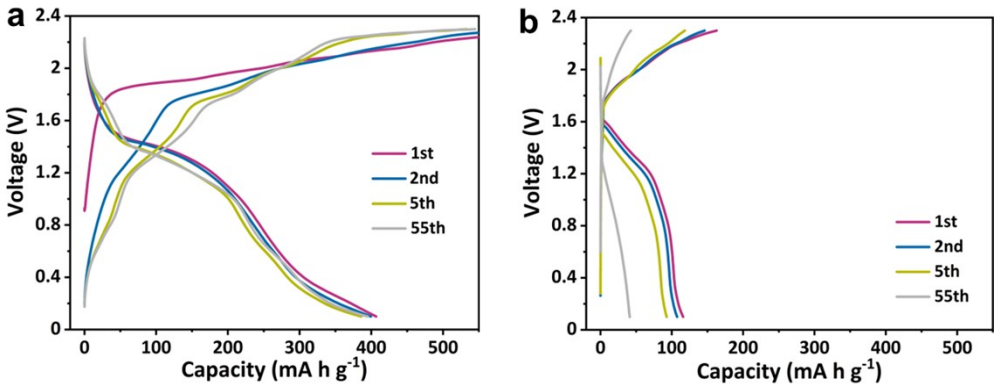

Fig. S11. The GCD curves of (a) $MoSe_2$ and (b) pure Se electrodes at 0.5 A g^{-1}.

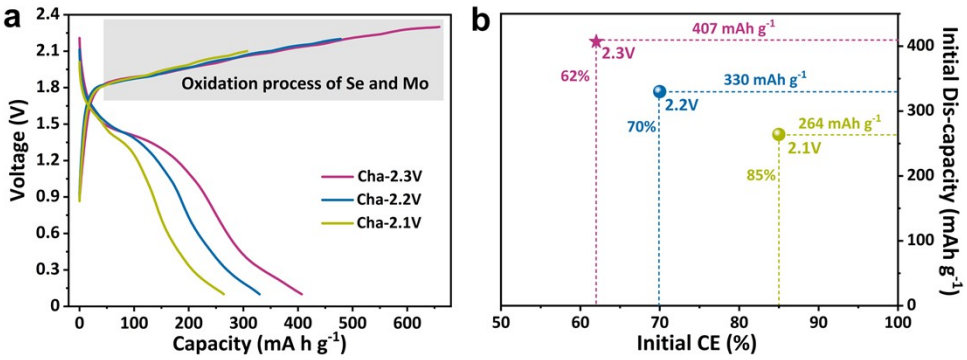

Fig. S12. The GCD curves of Zn-$MoSe_2$ batteries with different cut-off voltages. In our work, a slightly excessive Zn anode was used to couple with the cathode, thereby the capacity is calculated based on the loading mass of $MoSe_2$ cathode materials. Thus, the ICE should be associated with the reversibility of the cathode material and electrolyte stability rather than the Zn anode. To identify the origin of the low ICE, we conducted the battery tests in different cutoff voltages of 0.1-2.3, 0.1-2.2, and 0.1-2.1 V, and compared their GCD curves. As shown in Fig. S12, corresponding to the cutoff voltages of 0.1-2.3, 0.1-2.2, and 0.1-2.1 V, the ICE is 62%, 70%, and 85%, respectively. It confirms that the cutoff voltage greatly affects the ICE. Although the ICE can be remarkably enhanced by lowering the upper limit of cutoff voltage, an evident capacity decrease occurs (from 407 to 264 mA h g^{-1}) due to the incomplete oxidation conversion of Se and Mo, which is not beneficial to obtain a high energy density. Nevertheless, with the increase of current density, the ICE can be dramatically improved (Fig. 3c), suggesting that the low ICE issue can be effectively solved at relatively large current densities. Thus, in our work, we chose 0.1-2.3 V as the cutoff voltage for Zn-$MoSe_2$ batteries, which is beneficial to synchronously achieve a high CE and high discharge capacity.

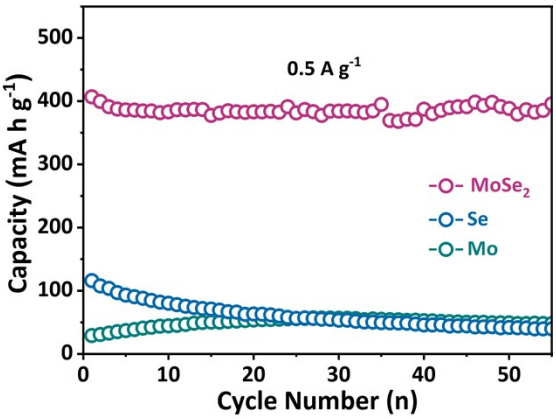

Fig. S13. The cycling performance of $MoSe_2$, pure Se, and pure Mo electrodes at 0.5 A g^{-1}.

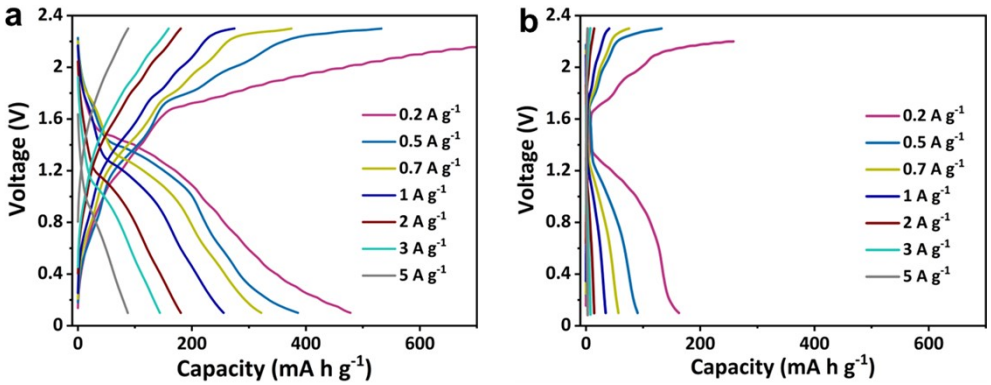

Fig. S14. The GCD curves of (a) $MoSe_2$ and (b) pure Se electrodes at different current densities.

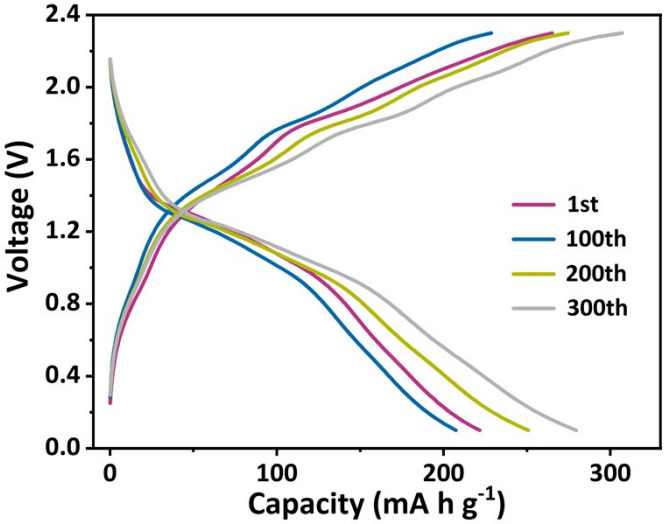

Fig. S15. The GCD curves of $MoSe_2$ electrode at 1 A g^{-1}.

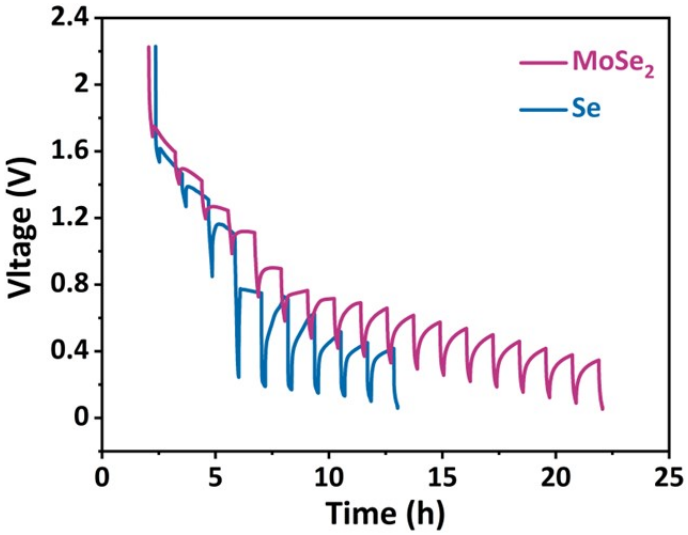

Fig. S16. The GITT plots of $MoSe_2$ and pure Se electrodes at the discharging state.

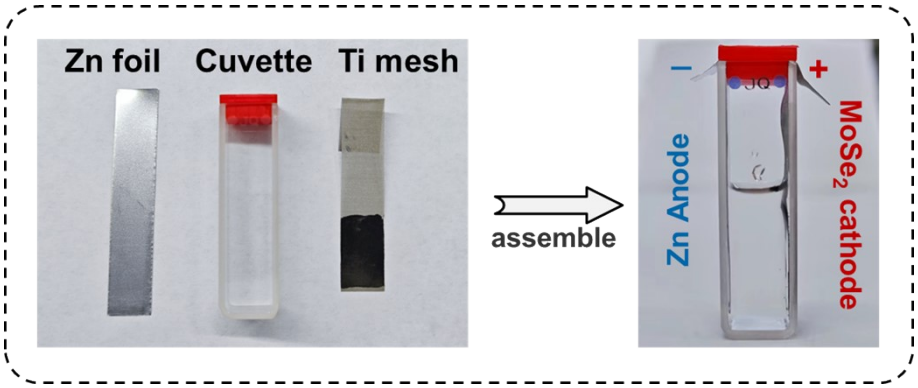

Fig. S17. The assembly schematic of the cuvette-type battery.

Fig. S18. The side view of the cuvette-type battery cycled.

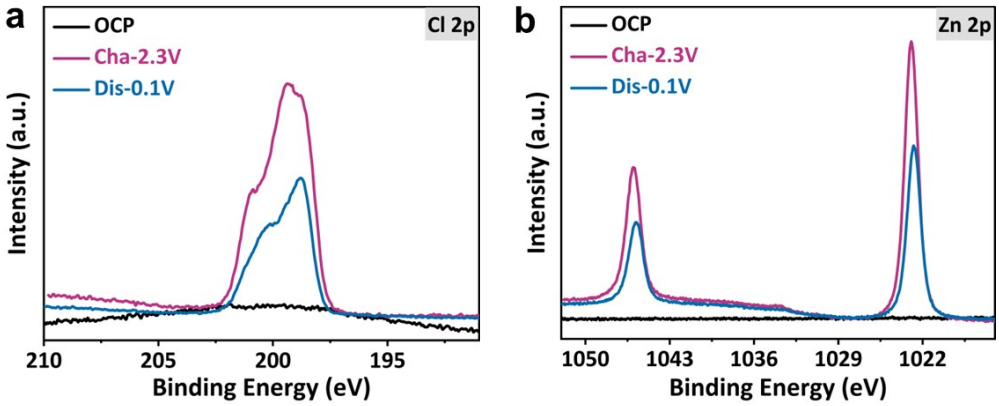

Fig. S19. The *ex-situ* XPS spectra of Cl 2p (a) and Zn 2p (b) of $MoSe_2$ electrode at different states.

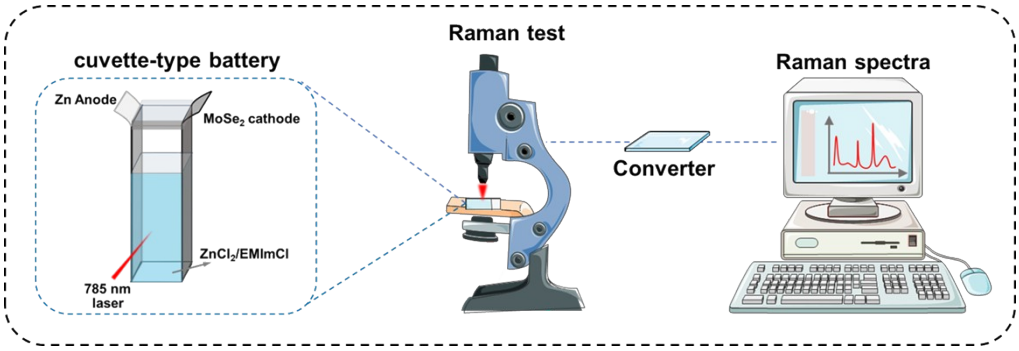

Fig. S20. The Raman test of $ZnCl_2$/EMImCl at different charged/discharged states.

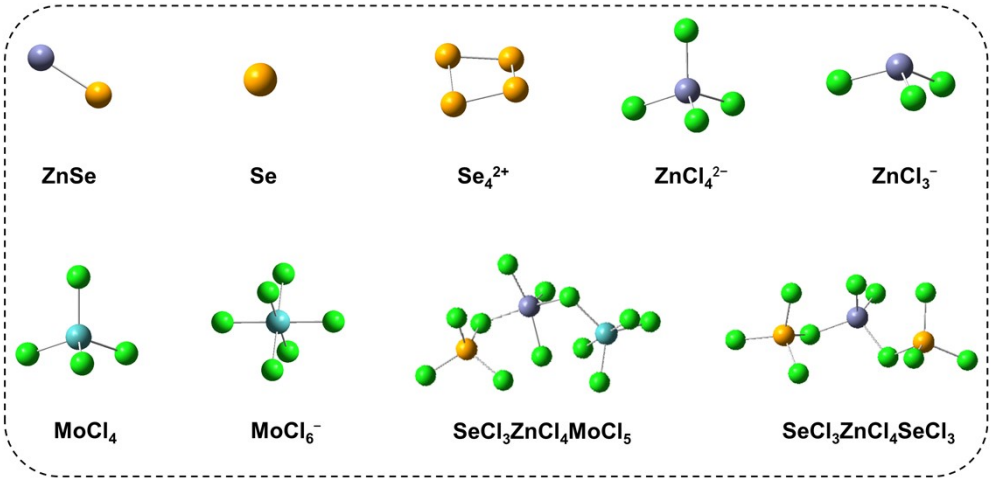

Fig. S21. The optimized theoretical structures of ZnSe, Se, Se_4^{2+}, $ZnCl_4^{2-}$, $ZnCl_3^-$, $MoCl_4$, $MoCl_6^-$, $SeCl_3ZnCl_4MoCl_5$ and $(SeCl_3)_2ZnCl_4$.

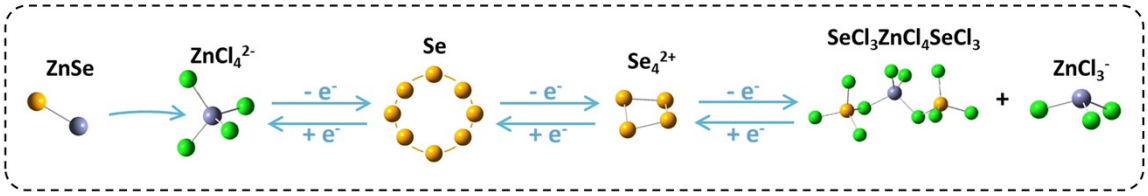

Fig. S22. The schematic illustrations of phase conversion of Zn-Se battery.

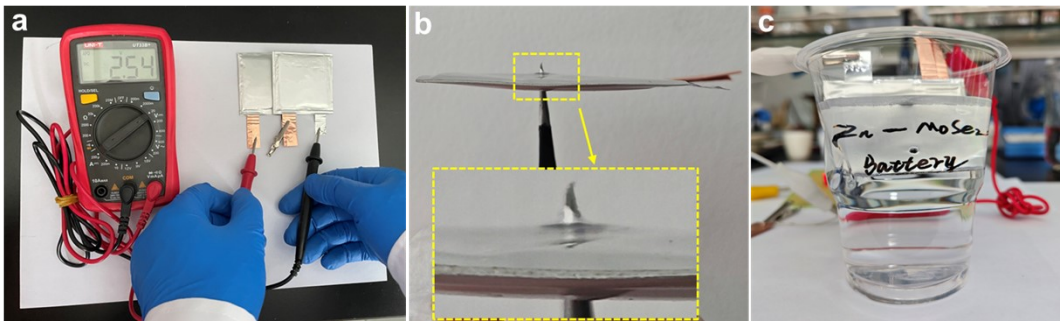

Fig. S23. (a) The photograph of the open circuit voltage of Zn-$MoSe_2$ batteries. (b) The photograph of the punctured battery. (c) The photograph of the cutting-off battery submerged in water.

3. Supplementary Tables

Table S1. Compared with analogical materials or systems reported previously.

Electrode (Battery)	Electrolyte	Discharge plateau	Low-rate capacity	High-rate capacity	Capacity Retention	Ref.
Te@CSs MIB (2032-coin)	$AlCl_3$/THF	1.0 V	387 mAh g^{-1} (0.1 A g^{-1})	165 mAh g^{-1} (5 A g^{-1})	77% after 500 cycles at 0.5 A g^{-1}	2
Se@CMK-3 AIB (Swagelok)	1 M ZnTFSI in EMC	~1.0 V	550 mAh g^{-1} (0.1 A g^{-1})	270 mAh g^{-1} (5 A g^{-1})	81.2% after 500 cycles at 1 A g^{-1}	3
TP-Se (2032-coin)	1 M $Zn(OTF)_2$	~1.85 V	317 mAh g^{-1} (0.5 A g^{-1})	138 mAh g^{-1} (30 A g^{-1})	85.3% after 4300 cycles at 2 A g^{-1}	4
NiTe AIB (Swagelok)	$AlCl_3$/EMImCl	1.25 V	450 mAh g^{-1} (0.2 A g^{-1})	210 mAh g^{-1} (1 A g^{-1})	68% after 100 cycles at 0.5 A g^{-1}	5
S/CNT AIB (2032-coin)	$AlCl_3$/ carbamide	1.8 V	162.5 mAh g^{-1} (0.2A g^{-1})	95 mAh g^{-1} (1 A g^{-1})	71.4% after 100 cycles at 1 A g^{-1}	6
$CoSe_2$@C AIB (Swagelok)	$AlCl_3$/EMImCl	~1.8V	200 mAh g^{-1} (1 A g^{-1})	98 mAh g^{-1} (1 A g^{-1})	67% after 600 cycles at 1 A g^{-1}	7
Se-CT AIB (Swagelok)	$AlCl_3$/EMImCl	1.78 V	450 mAh g^{-1} (0.2 A g^{-1})	170 mAh g^{-1} (0.5 A g^{-1})	80% after 200 cycles at 2 A g^{-1}	7
Se@pani@G AIB (Swagelok)	$AlCl_3$/EMImCl	1.65 V	344 mAh g^{-1} (0.2 A g^{-1})	-	32% after 400 cycles at 1 A g^{-1}	8
Red P AIB (Swagelok)	$AlCl_3$/EMImCl	~0.6 V	350 mAh g^{-1} (0.1 A g^{-1})	-	34% after 200 cycles at 0.1 A g^{-1}	9
Te AIB (pouch)	$AlCl_3$/EMImCl	~1.2 V	420 mAh g^{-1} (0.2 A g^{-1})	260 mAh g^{-1} (1 A g^{-1})	37.5% after 200 cycles at 0.5 A g^{-1}	10
$MoSe_2$@C AIB (pouch)	$AlCl_3$/EMImCl	~0.6 V	260 mAh g^{-1} (0.1 A g^{-1})	90 mAh g^{-1} (5 A g^{-1})	100% after 5000 cycles at 1 A g^{-1}	11
S-WSe_2 AIB (Swagelok)	$AlCl_3$/EMImCl	~1.5 V	350 mAh g^{-1} (0.1 A g^{-1})	110 mAh g^{-1} (2 A g^{-1})	68% after 1500 cycles at 2 A g^{-1}	12
$MoSe_2$ ZB (2032-coin)	$ZnCl_2$/EMImCl	~1.5 V	500 mAh g^{-1} (0.2 A g^{-1})	100 mAh g^{-1} (5 A g^{-1})	99% after 9000 cycles at 5 A g^{-1}	This Work

Table S2. The fitted EIS results before and after cycles.

Electrode	Cycle	R_{ct} (Ω)
Pure Se	Pristine	335
	50th	203
$MoSe_2$	Pristine	49
	50th	28

Table S3. Gibbs free energy of reactants and products calculated by DFT.

Component	G(eV)
Zn	-6181.720
Zn^{2+}	-6153.389
Se	-251.870
ZnSe	-6435.752
Se_4^{2+}	-996.539
$ZnCl_4^{2-}$	-56283.408
$ZnCl_3^-$	-43759.649
$MoCl_4$	-51954.933
$MoCl_6^-$	-77007.659
$SeCl_3ZnCl_4MoCl_5$	-158581.844
$(SeCl_3)_2ZnCl_4$	-131927.695

Table S4. The calibrated Gibbs free energies of the anionic products at different reaction paths.

Zn-Cl anions	$Zn_2Cl_6^{2-}$	$Zn_2Cl_5^-$	$Zn_3Cl_7^-$	$ZnCl_3^-$
deltaG/eV	-2.466	-2.154	-1.001	-6.654

For the reaction on the Zn-anode side, we have modeled the reaction paths of the possible Zn-Cl anions products by theoretical calculations and compared calibrated Gibbs free energies. As shown in Table R1, the Gibbs free energy for generating $ZnCl_3^-$ anion is much lower than that of other Zn-Cl anions, which demonstrates that the Zn anode is highly susceptible to the generation of $ZnCl_3^-$ in this system. In addition, only the signal of the $ZnCl_3^-$ anion instead of other Zn-Cl anions is detected in the ex-situ TOF-SIMS spectra (Fig. 4c). These results verify that the anode reaction during the charging/discharging processes is as follows:

$$Zn + ZnCl_4^{2-} \leftrightarrow ZnCl_3^- + e^-$$

4. Supplementary References

1. Chen, Z.; Yang, Q.; Wang, D.; Chen, A.; Li, X.; Huang, Z.; Liang, G.; Wang, Y.; Zhi, C., Tellurium: A High-Performance Cathode for Magnesium Ion Batteries Based on a Conversion Mechanism. *ACS Nano* **2022,** *16*, 5349-5357.
2. Chen, Z.; Mo, F.; Wang, T.; Yang, Q.; Huang, Z.; Wang, D.; Liang, G.; Chen, A.; Li, Q.; Guo, Y.; Li, X.; Fan, J.; Zhi, C., Zinc/selenium conversion battery: a system highly compatible with both organic and aqueous electrolytes. *Energy Environ. Sci.* **2021,** *14*, 2441-2450.
3. Chen, Z.; Cui, H.; Hou, Y.; Wang, X.; Jin, X.; Chen, A.; Yang, Q.; Wang, D.; Huang, Z.; Zhi, C., Anion chemistry enabled positive valence conversion to achieve a record high-voltage organic cathode for zinc batteries. *Chem* **2022,** *8*, 2204-2216.
4. Yu, Z.; Jiao, S.; Tu, J.; Luo, Y.; Song, W.-L.; Jiao, H.; Wang, M.; Chen, H.; Fang, D., Rechargeable Nickel Telluride/Aluminum Batteries with High Capacity and Enhanced Cycling Performance. *ACS Nano* **2020,** *14*, 3469-3476.
5. Li, H.; Meng, R.; Guo, Y.; Chen, B.; Jiao, Y.; Ye, C.; Long, Y.; Tadich, A.; Yang, Q.-H.; Jaroniec, M.; Qiao, S.-Z., Reversible electrochemical oxidation of sulfur in ionic liquid for high-voltage Al-S batteries. *Nat. Commun.* **2021,** *12*, 5714.
6. Hong, H.; Liu, J.; Huang, H.; Atangana Etogo, C.; Yang, X.; Guan, B.; Zhang, L., Ordered Macro-Microporous Metal-Organic Framework Single Crystals and Their Derivatives for Rechargeable Aluminum-Ion Batteries. *J. Am. Chem. Soc.* **2019,** *141*, 14764-14771.
7. Li, Z.; Liu, J.; Huo, X.; Li, J.; Kang, F., Novel One-Dimensional Hollow Carbon Nanotubes/Selenium Composite for High-Performance Al-Se Batteries. *ACS Appl. Mater. Interfaces* **2019,** *11*, 45709-45716.
8. Lei, H.; Tu, J.; Li, S.; Huang, Z.; Luo, Y.; Yu, Z.; Jiao, S., Graphene-encapsulated selenium@polyaniline nanowires with three-dimensional hierarchical architecture for high-capacity aluminum-selenium batteries. *J. Mater. Chem. A* **2022,** *10*, 15146-15154.
9. T. Cai, T. Li, B. Li, Y. Hu, X. Li, T. Lin, H. Hu, B. Luo, Y. Zhang, X. Zhu, Y. Cui, L. Zhao, W. Xing, Z. Yan, L. Wang, *Energy Storage Mater.* **2022**, 53, 415.
10. Zhao, Z.; Hu, Z.; Liang, H.; Li, S.; Wang, H.; Gao, F.; Sang, X.; Li, H., Nanosized $MoSe_2$@Carbon Matrix: A Stable Host Material for the Highly Reversible Storage of Potassium and Aluminum Ions. *ACS Appl. Mater. Interfaces* **2019,** *11*, 44333-44341.
11. Cui, F.; Han, M.; Zhou, W.; Lai, C.; Chen, Y.; Su, J.; Wang, J.; Li, H.; Hu, Y., Superlattice-Stabilized WSe_2 Cathode for Rechargeable Aluminum Batteries. *Small Methods* **2022,** *6*, 2201281.